Frontiers of Information Technology & Electronic Engineering
www.jzus.zju.edu.cn; engineering.cae.cn; www.springerlink.com
ISSN 2095-9184 (print); ISSN 2095-9230 (online)
E-mail: jzus@zju.edu.cn

Ultra-wideband FMCW ISAR imaging with a large rotation angle based on block-sparse recovery*

Ke JIN†‡, Tao LAI, Gong-quan LI, Ting WANG, Yong-jun ZHAO
(*Zhengzhou Institute of Information Science and Technology, Zhengzhou 450000, China*)
†E-mail: jk83302536@126.com

Received June 6, 2016; Revision accepted Nov. 28, 2016; Crosschecked Dec. 20, 2017

Abstract: Ultra-wideband frequency modulated continuous wave (FMCW) radar has the ability to achieve high-range resolution. Combined with the inverse synthetic aperture technique, high azimuth resolution can be realized under a large rotation angle. However, the range-azimuth coupling problem seriously restricts the inverse synthetic aperture radar (ISAR) imaging performance. Based on the turntable model, traditional match-filter-based, range Doppler algorithms (RDAs) and the back projection algorithm (BPA) are investigated. To eliminate the sidelobe effects of traditional algorithms, compressed sensing (CS) is preferred. Considering the block structure of a signal at high resolution, a block-sparsity adaptive matching pursuit algorithm (BSAMP) is proposed. By matching pursuit and backtracking, a signal with unknown sparsity can be recovered accurately by updating the support set iteratively. Finally, several experiments are conducted. In comparison with other algorithms, the results from processing the simulation data, some simple targets, and a complex target indicate the effectiveness and superiority of the proposed algorithm.

Key words: Frequency modulated continuous wave (FMCW); Inverse synthetic aperture radar (ISAR); Match-filter-based algorithm; Compressed sensing; Block sparsity
https://doi.org/10.1631/FITEE.1601310 **CLC number:** TN4

1 Introduction

Frequency modulated continuous wave (FMCW) radar has the advantages of light weight, low cost, and high resolution, compared with pulsed radar (Meta *et al.*, 2007). Thanks to dechirp processing, large instantaneous bandwidth can be achieved at a very low sampling rate. Combined with the inverse synthetic aperture radar (ISAR) technique, FMCW radar can implement 2D imaging on simple system architectures, thus becoming a powerful detection method for non-cooperative targets (Hu *et al.*, 2010) and showing tremendous value when applied in unmanned aerial vehicle (UAV) imaging and identification (Kim *et al.*, 2005).

To obtain a high-resolution and high-quality ISAR image, a large bandwidth for the transmitted signal and a large angular integration width are needed. Traditional range Doppler algorithms (RDAs) deal with small rotation angle imaging problems, which ignore range-azimuth coupling and will seriously defocus an ISAR image at a large angle (Xing *et al.*, 2004). In these cases, some algorithms have been proposed to solve the problem of scatterers' migration through resolution cells (MTRC), including the polar format algorithm (PFA), the keystone-formatting algorithm, and the back projection algorithm (BPA) (Özdemir, 2012). However, these match-filter (MF) based algorithms are inevitably limited by the time-frequency uncertainty principle, and therefore they can neither eliminate the sidelobe nor gain super resolution (Herman and Strohmer, 2009).

---

‡ Corresponding author

* Project supported by the National Natural Science Foundation of China (No. 41301481)

ORCID: Ke JIN, https://orcid.org/0000-0001-9902-806X

The theory of compressed sensing (CS) provides an avenue for ISAR imaging with super resolution. The CS exploits the sparsity property of a signal in the transform domain and recovers it without distortion, using the l_1-minimization approach (Elhamifar and Vidal, 2012; Li and Qi, 2014a; 2014b). Two classes of widely studied recovery algorithms are convex relaxation algorithms and greedy algorithms (Wang, *et al.*, 2012). The former transform nondeterministic polynomial (NP) hard l_0-optimizations into l_1-minimizations, which can be solved efficiently through the basis pursuit (BP) method or a gradient projection for sparse reconstruction (GPSR). Although high recovery accuracy can be obtained, complex calculations are needed. Greedy algorithms select correct atoms in the dictionary via the matching pursuit (MP) technique, and then the ISAR signal can be expressed as a linear combination of them (Li *et al.*, 2012). This kind of algorithm reaches a compromise between computing efficiency and recovery accuracy, and it includes the MP algorithm, the orthogonal matching pursuit (OMP) algorithm, and the subspace matching pursuit (SP) algorithm.

In conventional CS theory, the scatterers are thought to be distributed in any position. However, when the resolution is increased, scatterers on complex targets will span resolution cells and form a block structure. Taking this additional structure into account, block-sparse compressed sensing is more suitable for ISAR imaging with a large bandwidth and large rotation angle (Eldar *et al.*, 2010). In this study, we develop a Ku-band radar system at a 6.2 GHz bandwidth to implement ISAR imaging for a short range. Then, the important range-azimuth coupling problem is analyzed in the ISAR turntable model, followed by image processing of the BPA. To eliminate the sidelobes in MF-based algorithms and take the block structure into consideration, an ISAR imaging algorithm based on block-sparsity adaptive matching pursuit (BSAMP) is proposed. Given matching pursuit and backtracking, this algorithm can decide on the block sparsity adaptively and find the correct support set rapidly, thus achieving a super-resolution ISAR image. Finally, the simulation results and real data processing verify the effectiveness of the proposed algorithm. Through comparison with the MF-based algorithms and the traditional CS algorithm, our algorithm shows superiority in imaging performance and feasibility in practice.

2 Ku-band FMCW radar system

The Ku-band FMCW radar system with 6.2 GHz bandwidth is used to detect targets at a short range and a block diagram of the whole system is shown in Fig. 1.

As shown in Fig. 1, a homodyne architecture transceiver is adopted to simplify the engineering design. The triangular voltage can be generated by the direct digital synthesizer (DDS) method or the signal generator. Here, the DDS method is preferred for its favorable voltage linearity. The 6.2 GHz bandwidth for the system is realized by the yttrium iron garnet (YIG) oscillator. In contrast to voltage-controlled oscillators (VCOs), the output frequency of the YIG is controlled by the current. Therefore, a voltage adjustment circuit and a voltage-to-current conversion

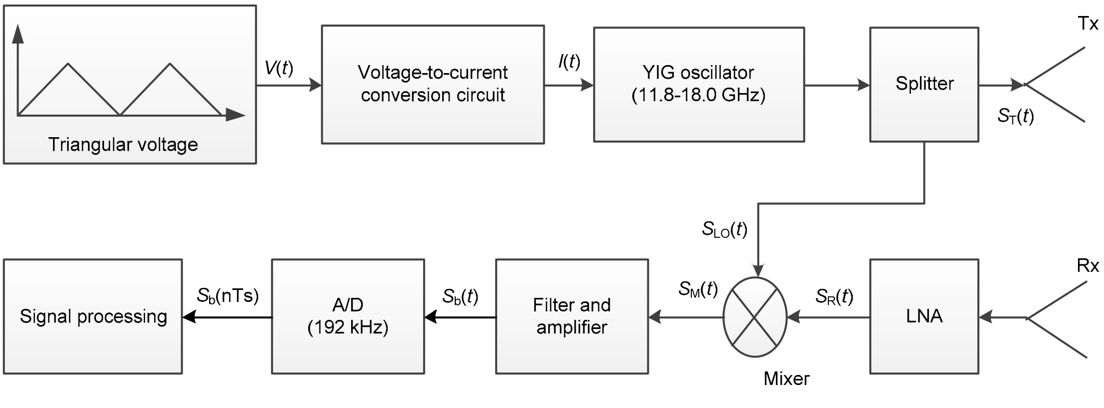

Fig. 1 Block diagram of the Ku-band FMCW radar system

circuit are required to produce the triangular current. The nonlinearity of the transmitted signal is about 8.2%. The specifications for the wideband radar system are listed in Table 1. Fig. 2 shows a photo of the Ku-band radar system.

Table 1 Specifications for the wideband FMCW radar system

Parameter	Value
Frequency	11.85–18.05 GHz
Pulse repetition interval	77.7 ms
Signal nonlinearity	8.2%
Modulation	Triangular FMCW
Transmitted power	16 dBm
Sampling rate	192 kHz
Resolution (theory)	2.42 cm
Detection range	180 m

Fig. 2 Photo of the Ku-band radar system

In this system, the signal generated by the YIG oscillator is divided into two parts: the transmitted signal and the local oscillator (LO) signal. The transmitted signal and LO signal can be written (amplitude is ignored) as

$$s_{\mathrm{T}}(t)=s_{\mathrm{LO}}(t)=\exp\{\mathrm{j}[2\pi(f_0 t+k_{\mathrm{r}}t^2/2)+\varepsilon(t)]\},\quad(1)$$

where f_0 is the central frequency, k_{r} is the chirp rate, t is the fast time, and $\varepsilon(t)$ is the nonlinear phase term. After being reflected by the targets, the received signal from N targets is the sum of a delayed version of $S_{\mathrm{T}}(t)$.

$$\begin{aligned}s_{\mathrm{R}}(t)=\sum\nolimits_{i=1}^{N}&\exp\{\mathrm{j}[2\pi(f_0(t-\tau_i)\\&+k_{\mathrm{r}}(t-\tau_i)^2/2)+\varepsilon(t-\tau_i)]\}.\end{aligned}\quad(2)$$

The dechirp method is applied to reduce the sampling rate in FMCW radar, so that the beat signal is the multiplication of the received signal and the LO signal. After the wideband mixer and low-pass filter, we may obtain the beat signal as

$$\begin{aligned}s_{\mathrm{b}}(t)=\sum_{i=1}^{N}\exp\Bigg\{\mathrm{j}\Bigg[2\pi\Bigg(&f_0\tau_i+\underbrace{+k_{\mathrm{r}}t\tau_i}_{\text{Target range}}\\&\underbrace{-k_r\tau_i^2/2}_{\text{RVP}}\Bigg)\underbrace{+\varepsilon(t)-\varepsilon(t-\tau_i)}_{\text{Nonlinearity}}\Bigg]\Bigg\}.\end{aligned}\quad(3)$$

According to the principle of FMCW radar ranging, the beat frequency $k_{\mathrm{r}}t\tau_i$ is proportional to the target's range, which can be measured accurately via the fast fourier transform (FFT). The residual video phase (RVP) term in Eq. (3) is neglected for short-range applications. The last nonlinear phase term varies with the target range and seriously deteriorates the range resolution by spreading the energy through different frequencies. To obtain a well-focused ISAR image, the nonlinearity in the beat signal is eliminated via the time-domain warping method (Middleton *et al.*, 2011; Anghel *et al.*, 2014; 2015) or match Fourier transform (Wang *et al.*, 2001; Fu *et al.*, 2012). For the remaining part of this paper, we will assume that the nonlinearity has been eliminated in the preprocessing stage.

The range of targets is measured by FFT and the azimuth dimension can be obtained through the relative motion between the radar and the targets.

3 ISAR turntable model and back projection algorithm

3.1 Signal model

Assume the translational motion has already been compensated for and the target is rotating uniformly with angular velocity ω. The sketch map is shown in Fig. 3. The range between the radar and rotation center is set to r_0 and the initial coordinates of the target are $(r_{\mathrm{p}}, \theta_{\mathrm{p}})$. Then, according to the cosine law, the range between the radar and the target is

$$r=\sqrt{r_0^2+r_{\mathrm{p}}^2+2r_0r_{\mathrm{p}}\sin(\theta_{\mathrm{p}}+\omega t_m)}, \tag{4}$$

where t_m is the slow time of m pulses. Substituting Eq. (4) into Eq. (3), the signal model can be expressed as

$$s(t,t_m)=\sigma\exp(\mathrm{j}(4\pi r/\lambda)+\mathrm{j}2\pi k_r t(2r/c)), \tag{5}$$

where λ is the wavelength and σ is proportional to the scatterer reflectivity. When $r_0 \gg r_p$, Eq. (4) can be Taylor expanded as

$$\begin{aligned} r(m) &\approx r_0+r_{\mathrm{p}}\sin(\theta_{\mathrm{p}}+\omega t_m) \\ &= r_0+y_p\cos(\omega t_m)+x_p\sin(\omega t_m), \end{aligned} \tag{6}$$

where x_p and y_p are the Cartesian coordinates of target P. In an RDA, the rotation angle is assumed to be small, so that $\cos(\omega t_m)\approx 1$, $\sin(\omega t_m)\approx 1$, and Eq. (5) can be approximated as (Lu and Bao, 1999; Zhang *et al.*, 2014)

$$\begin{aligned} s_{\mathrm{RD}}(t,t_m) &= \sigma_p\exp\left(\mathrm{j}4\pi\frac{r_0+y_p}{\lambda}\right) \\ &\quad\cdot\exp\left(\mathrm{j}2\pi\frac{2x_p\omega}{\lambda}t_m\right)\exp\left(\mathrm{j}2\pi k_r\frac{2(r_0+y_p)}{c}t\right). \end{aligned} \tag{7}$$

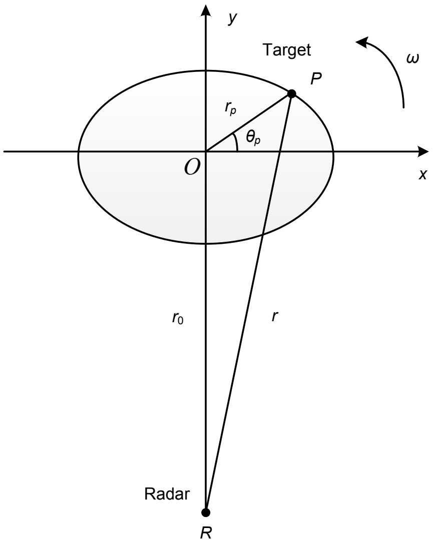

Fig. 3 ISAR turntable model

In this case, the range-azimuth coupling is separated and only the linear phase terms exist, so that a two-dimensional Fourier transform can be applied to separate targets and the ISAR image is obtained.

3.2 Back projection algorithm

In an RDA, two assumptions are employed to obtain the far-field small-rotation-angle ISAR image. When the target is detected at a short range (such as with a security check) or a high azimuth resolution is needed, the RDA will fail due to ignoring the serious range-azimuth coupling. A more accurate algorithm is the time-domain BPA.

In BPA, the information from the target's trajectory is naturally used, which makes it best suited when facing targets with highly nonlinear trajectories (Ribalta, 2011). The delay between the radar and targets is calculated, and then a coherent integration is applied to obtain a focused azimuth image, which can be written as

$$\hat{\sigma}_p=\sum_m W_{\mathrm{a}}(r;m)\exp\left(-\mathrm{j}\frac{4\pi r(m)}{\lambda}\right)S\left(\frac{2k_r}{c}r(m)\right), \tag{8}$$

where S is the Fourier transform of $s(t, t_m)$ and W_{a} is an azimuth windowing function.

In contrast to the RDA, the range between the radar and targets is accurately calculated. Thus, no approximation is used, which makes it suitable for short-range and large-angle ISAR imaging. Eq. (8) can be interpreted in three ways. First, the phase term $\exp(-\mathrm{j}4\pi r(m)/\lambda)$ compensates for the motion of targets, which varies as the target and rotation change. After that, a coherent integration works to increase the azimuth resolution. Second, it is a decoupling procedure. The term S is the pulse compression envelope denoting the range-azimuth coupling or the MTRC. The phase term first compensates for the range-dependent, second- and higher-order range-azimuth coupling terms, and then a Fourier transform works to integrate the linear azimuth phase to obtain a well-focused azimuth image (Wang *et al.*, 2010). Last, phase compensation is equivalent to the generalized match Fourier transform, which integrates the nonlinear phase term according to its variation. On the basis of the explanations above, the BPA is equivalent to the PFA or the keystone-formatting algorithm.

In an ISAR BPA, two inherent problems need to be solved: the range between the radar and the rotation center r_0 and the angular velocity ω. As the target is non-cooperative, r_0 and ω are not known. However, many methods have been proposed to estimate them. In this study, we use the minimum entropy to estimate the two parameters (Martorella *et al.*, 2005; Qiu and Zhao, 2006).

4 Block-sparsity adaptive matching pursuit algorithm

Limited by integration time, sidelobes in the MF-based algorithms are inevitable, affecting the image quality to some degree. In this case, compressed sensing emerges and solves this problem. On the other hand, when the radar resolution increases, complex scatterers will span across the resolution cells and become block targets. For this reason, the block-sparse-based compressed sensing algorithms are more suitable for ISAR super resolution imaging. In this study, we propose a BSAMP to conduct ISAR imaging with a wideband and large rotation angle. In an ISAR scenario, block sparsity is always unknown. Our proposed algorithm can find the optimal block sparsity through iteration and by updating the support set, under the condition of initial block sparsity and step length. After that, the image can be reconstructed rapidly and accurately.

4.1 Block-sparse model

Let $\boldsymbol{S}$ be the $M\times N$ data matrix of the ISAR echo and $\boldsymbol{\sigma}$ be the $K\times L$ matrix of reflectivity in the target spatial domain. Stack $\boldsymbol{S}$ and $\boldsymbol{\sigma}$ into a vector, i.e., $\boldsymbol{y}_{MN\times 1}=\mathrm{vec}(\boldsymbol{S})$, $\boldsymbol{x}_{KL\times 1}=\mathrm{vec}(\boldsymbol{\sigma})$. Considering the additional noise $\boldsymbol{n}$, the ISAR imaging model can be written as

$$\boldsymbol{y}=\boldsymbol{\Phi}\boldsymbol{x}+\boldsymbol{n}, \tag{9}$$

where $\boldsymbol{\Phi}$ is the $(MN)\times(KL)$ dictionary matrix. For k=1, 2, …, K and l=1, 2, …, L, we obtain KL sub-signals corresponding to all discretized spatial positions. After stacking them into an $(MN)\times(KL)$ matrix, $\boldsymbol{\Phi}$ can be written as $\boldsymbol{\Phi}=[\boldsymbol{y}_{11}, \boldsymbol{y}_{21}, \ldots, \boldsymbol{y}_{K1}, \boldsymbol{y}_{22}, \ldots, \boldsymbol{y}_{K2}, \ldots, \boldsymbol{y}_{2L}, \ldots, \boldsymbol{y}_{KL}]$.

In fact, the dictionary is a signal template for every time and every position of signal model (5). When implementing signal recovery, we manage to search for the most suitable unit in the dictionary. Once $\boldsymbol{x}$ is solved, an ISAR image of $K\times L$ is obtained.

The problem is that only a few strong scatterers exist in the scenario, which means only a few elements in $\boldsymbol{x}$ are nonzero and most are zero or near zero.

According to the theory of compressed sensing, solving the unknown vector $\boldsymbol{x}$ is to find the sparsest representation of a given signal, which can be expressed as an optimization program:

$$\min\|\boldsymbol{x}\|_0 \quad \text{s.t.} \quad \|\boldsymbol{y}-\boldsymbol{\Phi}\boldsymbol{x}\|_2\le\varepsilon, \tag{10}$$

where $\|\boldsymbol{x}\|_0$ is the l_0 norm of $\boldsymbol{x}$, which counts the number of nonzero elements in $\boldsymbol{x}$, and ε is the error tolerance threshold corresponding to the noise. The optimization program in Eq. (10) is NP-hard and has the restricted isometry property (RIP), which can be convex relaxed as (Wang *et al.*, 2011; Li and Qi, 2015)

$$\min\|\boldsymbol{x}\|_1 \quad \text{s.t.} \quad \|\boldsymbol{y}-\boldsymbol{\Phi}\boldsymbol{x}\|_2\le\varepsilon. \tag{11}$$

Methods have been proposed to solve Eq. (11), such as convex optimization and greedy algorithms.

The traditional sparse recovery model assumes that the elements in $\boldsymbol{x}$ are independent. In practice, however, there are some structural characteristics between the elements. The recovery performance will be increased if we take the signal correlation and structural characteristics as prior information. The commonly used structural feature is the block structure, which means there are q blocks in $\boldsymbol{x}$ and each block $\boldsymbol{x}_i$ contains d_i elements, i.e.,

$$\boldsymbol{x}=[\underbrace{\boldsymbol{x}_1,\cdots,\boldsymbol{x}_{d_1}}_{\boldsymbol{x}_1^{\mathrm{T}}},\cdots,\underbrace{\boldsymbol{x}_{d_{q-1}+1},\cdots,\boldsymbol{x}_{d_q}}_{\boldsymbol{x}_q^{\mathrm{T}}}]^{\mathrm{T}}. \tag{12}$$

Corresponding to sparsity, block sparsity means that only a few blocks in $\boldsymbol{x}$ are nonzero. To simplify the problem, we assume that every block has the same length, i.e., d_i=d. When d=1, block sparsity turns into the general sparse problem.

Furthermore, the dictionary can be divided into q blocks as

$$\boldsymbol{\Phi}=[\underbrace{\boldsymbol{\varphi}_1,\cdots,\boldsymbol{\varphi}_d}_{\boldsymbol{\Phi}_1^{\mathrm{T}}},\cdots,\underbrace{\boldsymbol{\varphi}_{(q-1)d+1},\cdots,\boldsymbol{\varphi}_{qd}}_{\boldsymbol{\Phi}_q^{\mathrm{T}}}]^{\mathrm{T}}. \tag{13}$$

In this case, solving the unknown vector $\boldsymbol{x}$ becomes the optimization program below:

$$\min \|\boldsymbol{x}\|_{2,0} \quad \text{s.t.} \quad \|\boldsymbol{y}-\boldsymbol{\Phi}\boldsymbol{x}\|_2 \le \varepsilon, \tag{14}$$

where $\|\boldsymbol{x}\|_{2,0}$ counts the number of nonzero blocks, or the blocks with nonzero l_2 norm. Methods as diverse as group lasso, group basis pursuit, and the mixed l_2/l_1 program (Li *et al.*, 2012) have been adopted previously to recover the signal.

4.2 Reconstruction algorithm

In considering the sparsity adaptive matching pursuit (SAMP) algorithm (Do *et al.*, 2008), the proposed BSAMP algorithm (Algorithm 1) can implement signal recovery under unknown block sparsity. On the other hand, the excellent recovery performance and high efficiency of block-sparse algorithms are retained in this algorithm.

Algorithm 1 Novel block-sparsity adaptive matching pursuit (BSAMP)

Input: echo vector $\boldsymbol{y}$, dictionary matrix $\boldsymbol{\Phi}$, block length d, and step size b_0.

Output: reconstructed signal $\hat{\boldsymbol{x}}$.

Step 1: initialization. Set $\hat{\boldsymbol{x}}=0$ and initialize residue $\boldsymbol{r}_0=\boldsymbol{y}$, initial block sparsity $L=b_0$, stage index stage=1, and finalist $\boldsymbol{F}_0=\varnothing$.

Step 2: preliminary test. The index set $\boldsymbol{S}_j$, i.e., $\boldsymbol{S}_j=\max(\|\boldsymbol{\Phi}_i^{\mathrm{T}} r_{j-1}\|, L)$, forms according to the index of the L largest projection value in the jth ($j=1, 2, \ldots, q$) iteration. This projection procedure can be implemented through the inner product and l_2 norm.

Step 3: making a candidate list. The candidate list $\boldsymbol{C}_j$ is the union of the finalist $\boldsymbol{F}_{j-1}$ and the index set $\boldsymbol{S}_j$, i.e., $\boldsymbol{C}_j=\boldsymbol{F}_{j-1}\cup\boldsymbol{S}_j$.

Step 4: final test. Obtain the support block set $\boldsymbol{F}$ through the least squares method, i.e., $\boldsymbol{F}=\max(\|\boldsymbol{\Phi}_{C_j}^{\dagger}\boldsymbol{y}\|_2, L)$, where $\boldsymbol{\Phi}_{C_j}^{\dagger}$ is the pseudo-inverse of $\boldsymbol{\Phi}_{C_j}$ and $\boldsymbol{\Phi}_{C_j}^{\dagger}=\left(\boldsymbol{\Phi}_{C_j}^{\mathrm{T}}\boldsymbol{\Phi}_{C_j}\right)^{-1}\boldsymbol{\Phi}_{C_j}^{\mathrm{T}}$. $\boldsymbol{\Phi}_{C_j}$ is a matrix consisting of the blocks from $\boldsymbol{\Phi}$ corresponding to the candidate list.

Step 5: computing the residue. With the supports noted above, the residue can be computed via the least squares method as $\boldsymbol{r}=\boldsymbol{y}-\boldsymbol{\Phi}_F\boldsymbol{\Phi}_F^{\dagger}\boldsymbol{y}$.

Step 6: adjusting block sparsity. If $\|\boldsymbol{r}\|_2 \ge \|\boldsymbol{r}_{j-1}\|_2$, then stage=stage+1, L=stage×L, and turn to step 2; else, $\boldsymbol{F}_j=\boldsymbol{F}$, $\boldsymbol{r}_j=\boldsymbol{r}$, $j=j+1$.

Step 7: reconstruction. If $j>q$ or the halting condition is true, i.e., $\|\boldsymbol{r}\|_2<\varepsilon$, then quit the iteration. The reconstructed signal is $\hat{\boldsymbol{x}}=\boldsymbol{\Phi}_F^{\dagger}\boldsymbol{y}$.

As described in the SAMP algorithm, sparsity k does not have to be known in our proposed algorithm, which is, in practice, more realistic. Given the initial block sparsity and step size, the finalist can be obtained through iteration and adjusting the block sparsity adaptively. By using backtracking as step 3, there is not just one support set that is found in the process of projection. In addition, the support set is updated and corrected at every iteration step, as shown in step 4; thus, a better reconstruction performance is realized. The basic procedure for the BSAMP algorithm is summarized in Fig. 4.

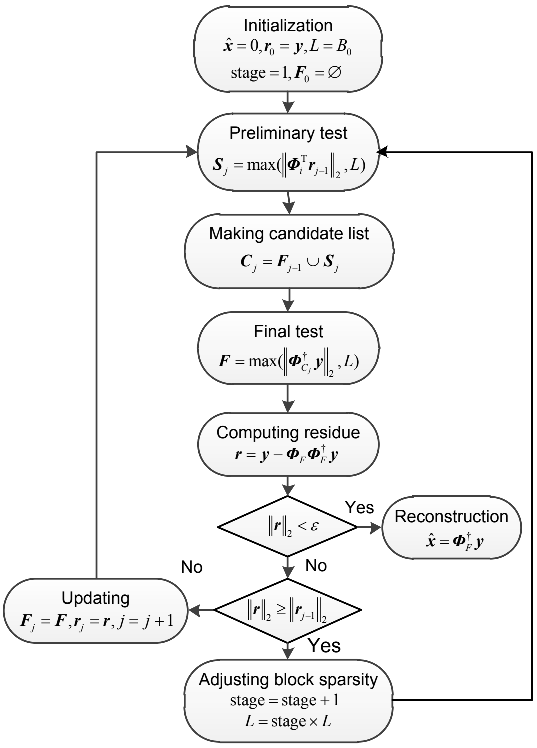

Fig. 4 Flowchart of the proposed algorithm

4.3 Computation cost

Unlike conventional block-sparsity recovery algorithms, such as block OMP (BOMP), our proposed algorithm uses an iteration operation, which means that the computation cost depends on the initial block sparsity L. It is easy to understand that when $L=1$, we need about K iterations to recover the signal with block sparsity K, i.e., $O(K)$. When we choose $L=K$, the number of iterations is about $\log K$, i.e., $O(\log K)$. In addition, the computation cost of each iteration lies mainly in the preliminary test procedure.

If the measurement matrix $\boldsymbol{\Phi}\in\mathbb{R}^{m\times N}$, then the computation complexity is between $O(mN\log K)$ and $O(mNK)$. Thus, advantages can be found in the computation complexity of our algorithm compared with the BOMP algorithm with $O(mNK)$ and the BPA with $O(N^3)$ (Ribalta, 2011).

5 Simulation and measurement results

In this section, simulations and real data processing results are used to validate the proposed BSAMP algorithm. This section will be divided into two parts. Part one contains the simulations and theoretical analysis, which shows the superiority of the proposed algorithm by comparison with MF-based algorithms and traditional CS algorithms. The second part contains the ISAR images of the corner reflectors and a model airplane, which validates the algorithm's feasibility with real data.

5.1 Simulation results

To simulate the actual signal, the simulation is conducted under the specifications of the aforementioned wideband FMCW radar system. The frequency range is 11.85–18.05 GHz, with a bandwidth of 6.2 GHz, which means the theoretical range resolution is 2.4 cm. The period of the linear frequency modulated (LFM) signal is 77.7 ms. Assume that the azimuth resolution is equal to the range resolution, and then the rotation angle is 23.8°. The angular velocity is set to 0.02 rad/s. Finally, the beat signal is sampled at a 192 kHz sampling rate.

In the first simulation, nine point targets are distributed in the scene at about 5 m to the radar, as shown in Fig. 5a. The ISAR images formed by MF-based algorithms and CS algorithms are shown in Figs. 5b–5f.

In Fig. 5b, only the target in the center of the turntable is well focused and the other targets are badly degraded for the far-field small-rotation-angle approximation of the RDA. In comparison, a serious range-azimuth coupling is taken into consideration and no approximations are employed in the PFA and BPA. Hence, better-focused ISAR images are obtained. The difference between these two methods is the numerical interpolation in the PFA, which can be neglected if it is well designed. However, the sidelobe still affects the image quality in high-resolution ISAR imaging. In Figs. 5e and 5f, we can recover the ISAR images with the OMP and only one scatterer in a point target, and the block length is d=1. Thus, there is nearly no difference reflected between Figs. 5e and 5f.

The next simulation is based on a model plane composed of many point scatterers, where some scatterers are gathered in a resolution cell and show some characteristics of agglomeration. A simulation based on the parameters above is shown in Fig. 6.

According to the analysis, the plane is badly degraded in Fig. 6b. With the help of PFA and BPA, the ISAR images in Figs. 6c and 6d are focused well, but the scatterers in a resolution cell cannot be separated and the images are contaminated by the sidelobe. When using the OMP algorithm, not only the outlines of the plane but also some false points are shown in Fig. 6e. The problem with the OMP algorithm can be interpreted as two factors. First, the OMP algorithm neglects the block structure of the signal, which leads to deterioration in the recovery performance. Second, the sparsity (k=170) is relatively large in the scenario, resulting in a decreased reconstruction rate. In comparison, with the block-sparse property, the signal can be recovered better and the reconstruction rate is higher even with the same sparsity (Wang *et al.*, 2012), as shown in Fig. 6f.

5.2 Real data results

Using the Ku-band FMCW radar system, measurements on real targets were conducted. In the first experiment, five corner reflectors were used to verify the advantage of CS algorithms over MF-based algorithms. In the scene, the corner reflectors are located about 3 m away from the radar antenna and supported by a foam cylinder. The turntable is driven by a step motor with an angular velocity of about 0.02 rad/s. After calculation, the rotation angle is 23.3°, corresponding to the theoretical azimuth resolution of 2.46 cm. The scenario photo and ISAR images of the experiment are shown in Fig. 7.

The RDA image (Fig. 7b) was seriously distorted by the range-azimuth coupling. However, better performance could be achieved with the PFAs and BPAs. Compared to the images in Figs. 7c and 7d, we may find that some strong sidelobes exist in the PFA and the focusing ability is inferior to that of the BPA

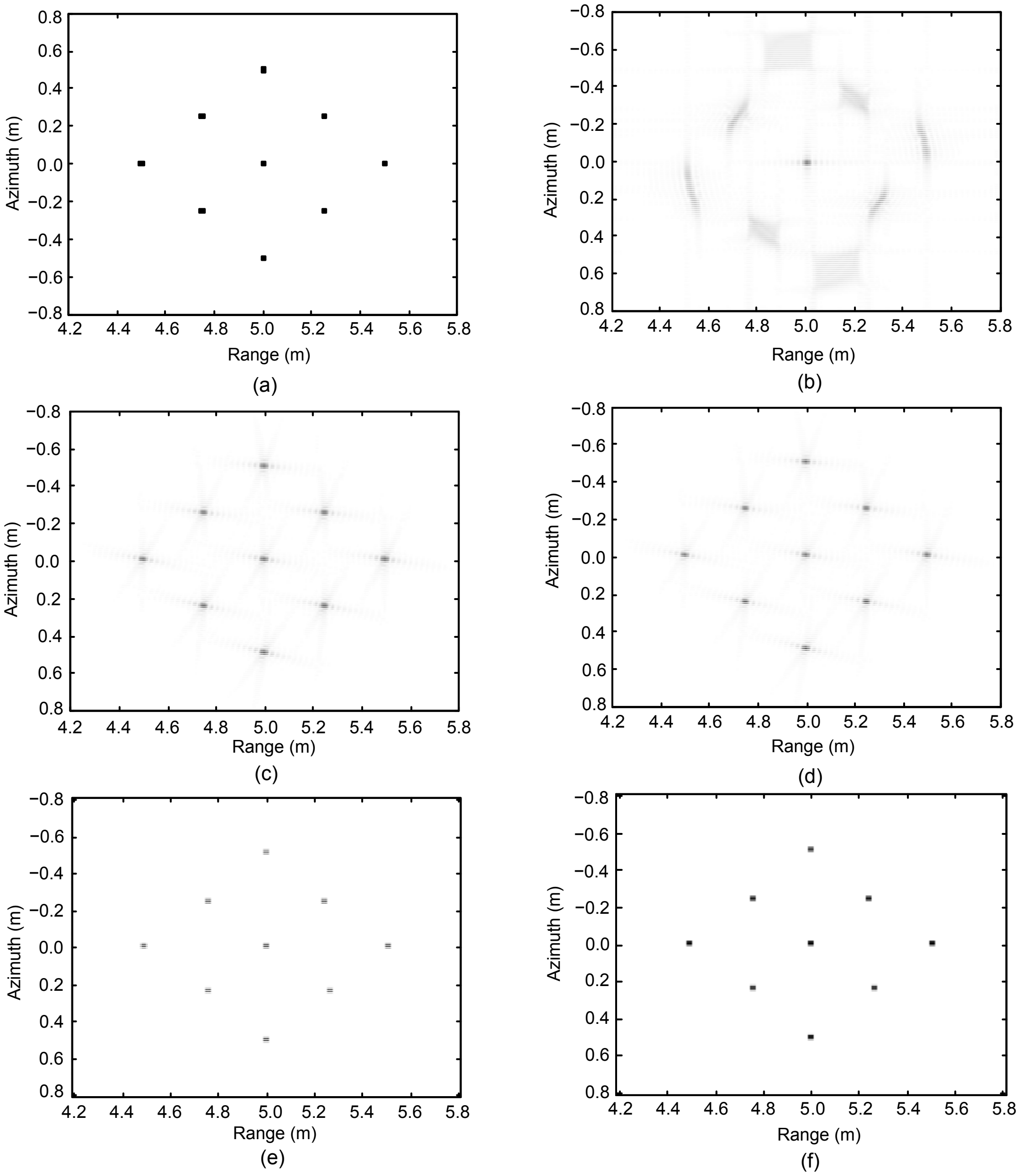

(a) (b) (c) (d) (e) (f)

Fig. 5 Point target simulations: (a) target locations; (b) ISAR image with RDA; (c) ISAR image with PFA; (d) ISAR image with BPA; (e) ISAR image with the OMP algorithm; (f) ISAR image with the BSAMP algorithm

due to its numerical operations. Though the sparsity is *k*=5, we cannot obtain five targets with the OMP algorithm because the corner reflectors are not ideal points. In contrast, the result is correct in our proposed algorithm. In fact, the step motor is another target, except for the corner reflectors, detected by the BSAMP algorithm, and the block sparsity is *k*=6.

In the following experiment, a model airplane was used to represent a complex target to be detected. The plane was placed about 3 m away from the radar and put on a foam cylinder. The length of the plane was 110 cm with an effective wingspan of 120 cm. The system parameters were the same as those used in the experiment above. The scenario photo and ISAR images are shown in Fig. 8.

Similar to the analysis above, some important scatterers on the airplane were distorted in Fig. 8b. In Figs. 8c and 8d, the nose, wings, tires, and engine can

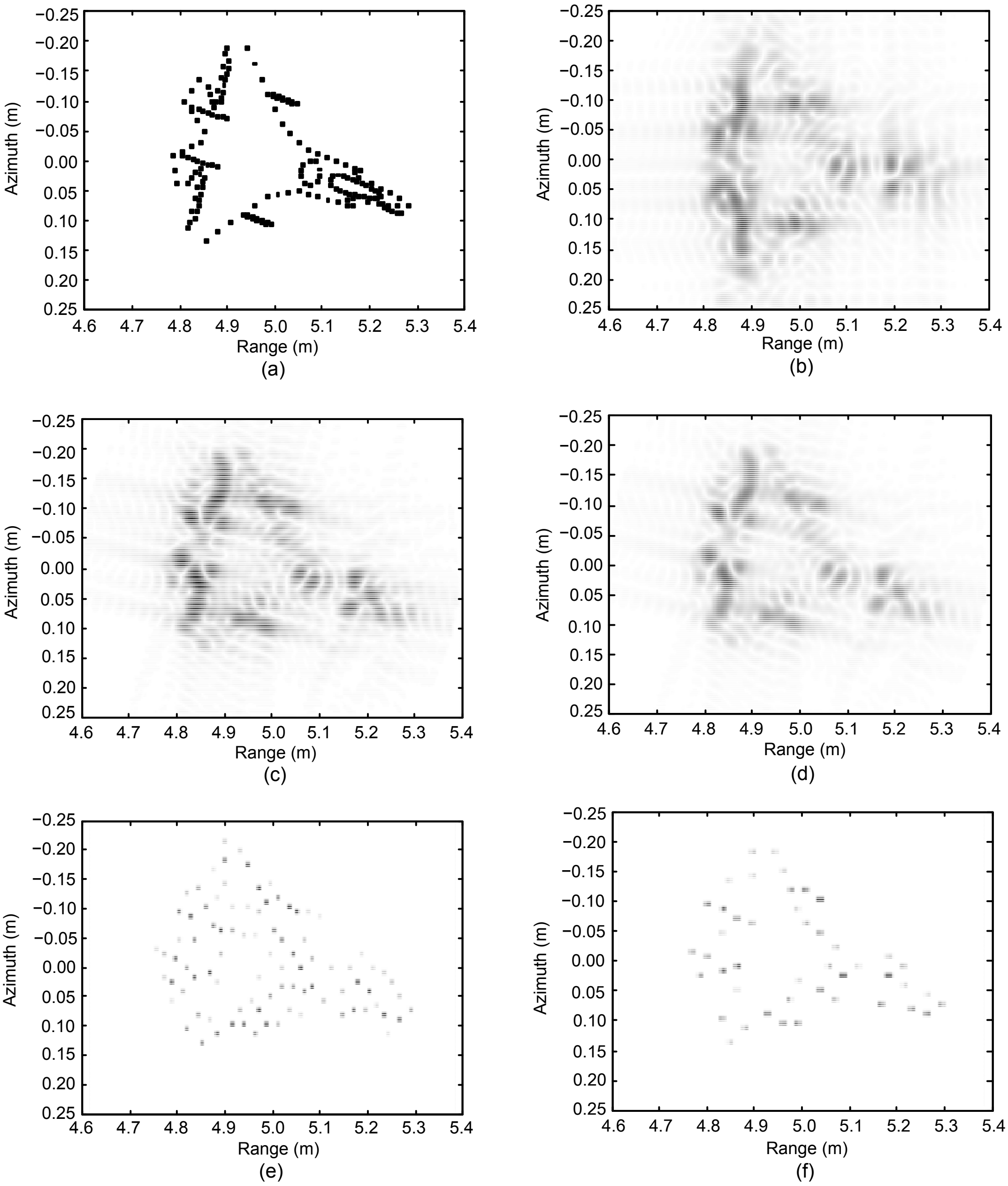

Fig. 6 Model plane simulations: (a) target locations; (b) ISAR image with RDA; (c) ISAR image with PFA; (d) ISAR image with BPA; (e) ISAR image with the OMP algorithm; (f) ISAR image with the BSAMP algorithm

be recognized easily. With the OMP algorithm, we can see that the outlines were combined with some false targets, corresponding to the simulations in Section 5.1. What is different from the simulations and the corner reflectors in this experiment is that the sparsity is unknown. In this way, our proposed algorithm has a natural advantage in signal recovery. Attributed to the property of block sparsity, the important components on the plane could be distinguished clearly with no influence from the sidelobe and false targets. What is more, the more subtle the division of the grid, the higher the resolution obtained of the image, at the cost of increasing the amount of calculation and memory. This experiment also shows that ultra-wideband FMCW radar can be used for high-resolution identification of low-altitude targets such as UAVs.

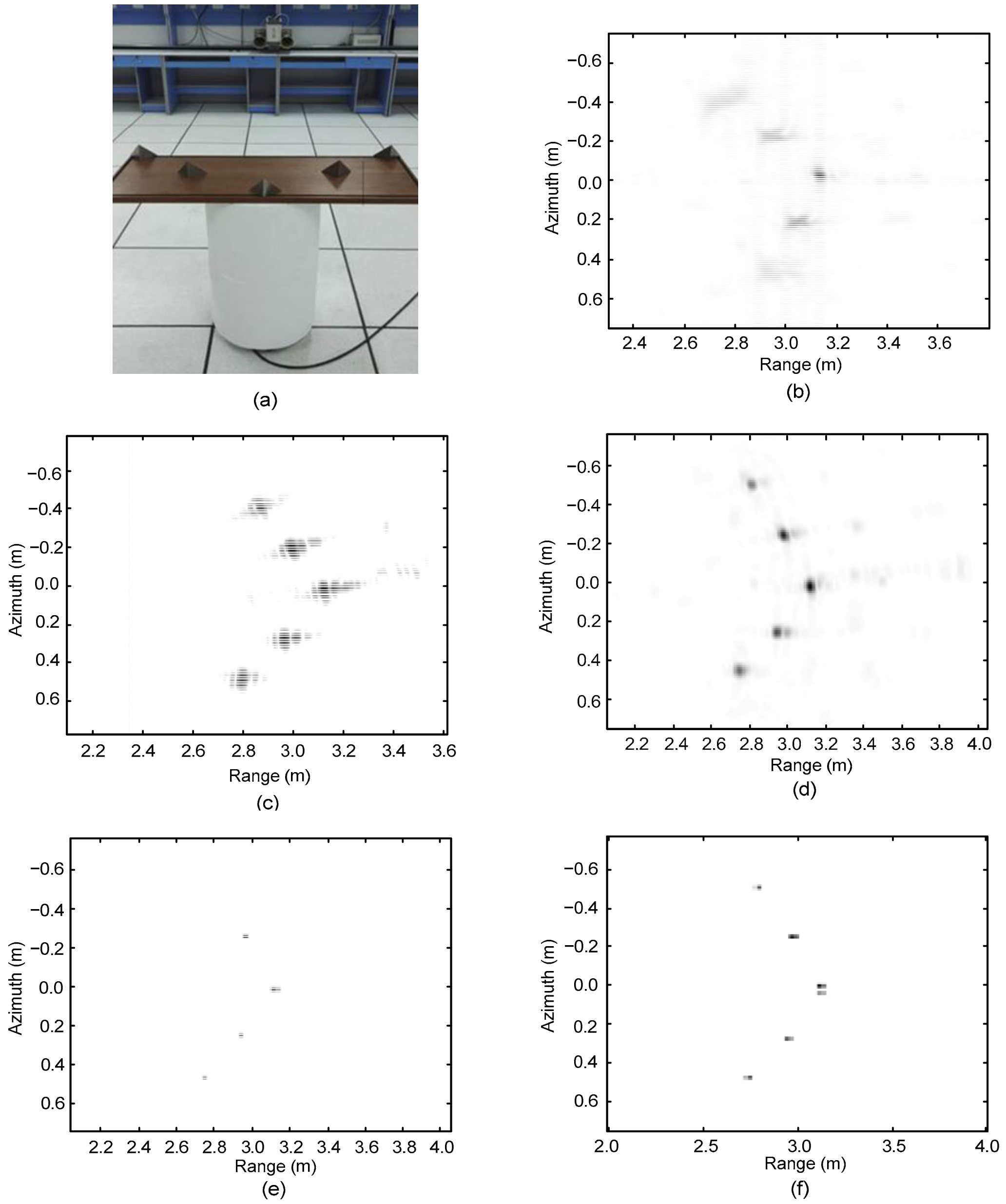

(a) (b) (c) (d) (e) (f)

Fig. 7 Corner reflector experiments: (a) photo of the scenario; (b) ISAR image with RDA; (c) ISAR image with PFA; (d) ISAR image with BPA; (e) ISAR image with the OMP algorithm; (f) ISAR image with the BSAMP algorithm

6 Conclusions

In this paper, we studied ISAR imaging with a large rotation angle. The important range-azimuth coupling was analyzed in the turntable model. To solve the problem of sidelobe effects in MF-based algorithms, compressed sensing was used. Considering the block-sparse property at high resolution and unknown sparsity, we proposed the block-sparsity adaptive matching pursuit algorithm. With a higher reconstruction rate and without artificial settings, the proposed algorithm was tested with simulations and real targets. The results demonstrated its superiority to MF-based and traditional CS algorithms. Future work is needed to improve the anti-noise performance of block-sparse algorithms.

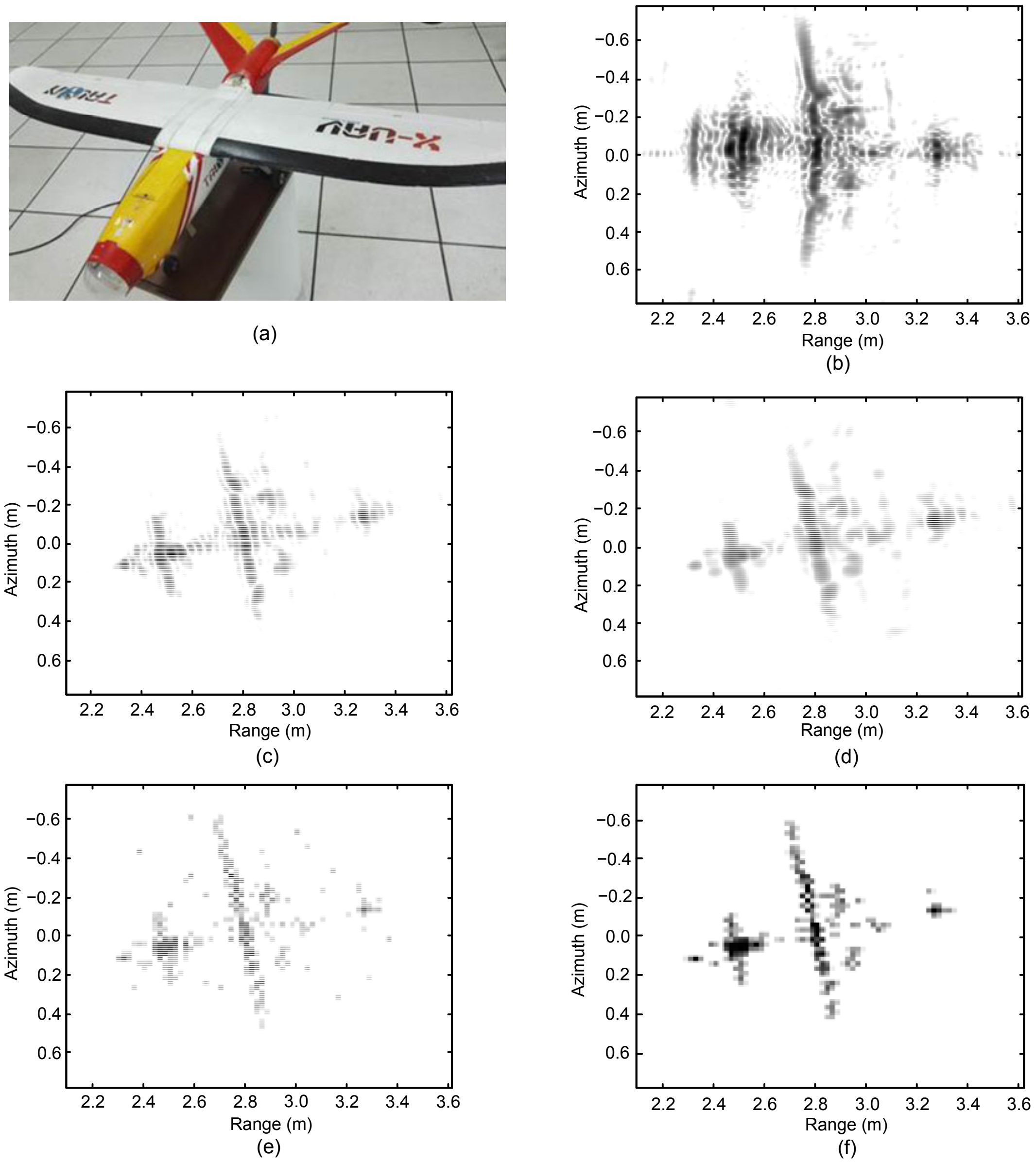

Fig. 8 Model airplane experiments: (a) photo of the plane; (b) ISAR image with RDA; (c) ISAR image with PFA; (d) ISAR image with BPA; (e) ISAR image with the OMP algorithm; (f) ISAR image with the BSAMP algorithm

References

Anghel, A., Vasile, G., Cacoveanu, R., *et al*., 2014. Short-range wideband FMCW radar for millimetric displacement measurements. *IEEE Trans. Geosci. Remote Sens*., **52**(9):5633-5642. https://doi.org/10.1109/TGRS.2013.2291573

Anghel, A., Vasile, G., Cacoveanu, R., *et al*., 2015. Range autofocusing for FMCW radars using time warping and a spectral concentration measure. IEEE Radar Conf., p.581-586. https://doi.org/10.1109/RADAR.2015.7131065

Do, T.T., Gan, L., Nguyen, N., *et al*., 2008. Sparsity adaptive matching pursuit algorithm for practical compressed sensing. 42nd Asilomar Conf. on Signals, p.581-587. https://doi.org/10.1109/ACSSC.2008.5074472

Eldar, Y.C., Kuppinger, P., Bolcskei, H., 2010. Block-sparse signals: uncertainty relations and efficient recovery. *IEEE Trans. Signal Process*., **58**(6):3042-3054. https://doi.org/10.1109/TSP.2010.2044837

Elhamifar, E., Vidal, R., 2012. Block-sparse recovery via convex optimization. *IEEE Trans. Signal Process*., **60**(8):4094-4107. https://doi.org/10.1109/TSP.2012.2196694

Fu, Y.W., Li, Y.N., Li, X., 2012. A 3D InISAR imaging method for non-uniformly rotating target based on match. *Four. Transf. J. Astron*., **33**(6):769-775 (in Chinese). https://doi.org/10.3873/j.issn.1000-1328.2012.06.012

Herman, M.A., Strohmer, T., 2009. High-resolution radar via compressed sensing. *IEEE Trans. Signal Process.*, **57**(6): 2275-2284. https://doi.org/10.1109/TSP.2009.2014277

Hu, J.M., Jiang, W.D., Fu, Y.W., *et al.*, 2010. A novel range alignment algorithm for ISAR. IEEE 2nd Int. Conf. on Computer Engineering and Technology, p.358-362. https://doi.org/10.1109/ICCET.2010.5486064

Kim, K.T., Seo, D.K., Kim, H.T., 2005. Efficient classification of ISAR images. *IEEE Trans. Antennas Propag.*, **53**(5): 1611-1621. https://doi.org/10.1109/TAP.2005.846780

Li, G., Zhang, H., Wang, X.Q., *et al.*, 2012. ISAR 2D imaging of uniformly rotating targets via matching pursuit. *IEEE Trans. Aerosp. Electron. Syst.*, **48**(2):1838-1846. https://doi.org/10.1109/TAES.2012.6178106

Li, S.J., Qi, H.R., 2014a. Compressed dictionary learning for detecting activations in fMRI using double sparsity. IEEE Global Conf. on Signal and Information Processing, p.434-437. https://doi.org/10.1109/GlobalSIP.2014.7032154

Li, S.J., Qi, H.R., 2014b. Recursive low-rank and sparse recovery of surveillance video using compressed sensing. Proc Int. Conf. on Distributed Smart Cameras, Article 1. https://doi.org/10.1145/2659021.2659029

Li, S.J., Qi, H.R., 2015. A Douglas-Rachford splitting approach to compressed sensing image recovery using low-rank regularization. *IEEE Trans. Image Process.*, **24**(11): 4240-4249. https://doi.org/10.1109/TIP.2015.2459653

Lu, G.Y., Bao, Z., 1999. Analysis of MTRC compensation algorithm in ISAR. IEEE Radar Conf., p.242-245. https://doi.org/10.1109/NRC.1999.767330

Martorella, M., Berizzi, F., Haywood, B., 2005. Contrast maximisation based technique for 2D ISAR autofocusing. *IEE Proc. Radar Son. Navig.*, **152**(4):253-262. https://doi.org/10.1049/ip-rsn:20045123

Meta, A., Hoogeboom, P., Ligthart, L.P., 2007. Signal processing for FMCW SAR. *IEEE Trans. Geosci. Remote Sens.*, **45**(11):3519-3532. https://doi.org/10.1109/TGRS.2007.906140

Middleton, R.J.C., Macfarlane, D.G., Robertson, D.A., 2011. Range autofocus for linearly frequency-modulated continuous wave radar. *IET Radar Sonar Navig.*, **5**(3):288-295. https://doi.org/10.1049/iet-rsn.2010.0097

Özdemir, C., 2012. Inverse synthetic aperture radar imaging with MATLAB algorithms. John Wiley & Sons, Hoboken, New Jersey, America. https://doi.org/10.1002/9781118178072

Qiu, X.H., Zhao, Y., 2006. A non-parametric rotating angle acquisition method for optimal ISAR imaging. IEEE Antennas and Propagation Society Int. Symp., p.2697-2700. https://doi.org/10.1109/APS.2006.1711159

Ribalta, A., 2011. Time-domain reconstruction algorithms for FMCW-SAR. *IEEE Geosci. Remote Sens. Lett.*, **8**(3):396-400. https://doi.org/10.1109/LGRS.2010.2078486

Wang, H.X., Liang, Y., Xing, M.D., *et al.*, 2011. ISAR imaging via sparse frequency-stepped chirp signal. *Sci. China Inform.*, **55**(4):877-888. https://doi.org/10.1007/s11432-011-4353-1

Wang, R., Loffeld, O., Nies, H., *et al.*, 2010. Focus FMCW SAR data using the wavenumber domain algorithm. *IEEE Trans. Geosci. Remote Sens.*, **48**(4):2109-2118. https://doi.org/10.1109/TGRS.2009.2034368

Wang, S.L., Li, S.G., Ni, J.L., *et al.*, 2001. A new transform-match Fourier transform. *Acta Electron. Sin.*, **29**(3):403-405 (in Chinese). https://doi.org/10.3321/j.issn:0372-2112.2001.03.030

Wang, W.W., Liao, G.S., Zhang, L., *et al.*, 2012. An imaging method based on compressive sensing for sparse aperture of SAR. *Acta Electron. Sin.*, **40**(12):2487-2494 (in Chinese). https://doi.org/10.3969/j.issn.0372-2112.2012.12.021

Xing, M.D., Wu, R.B., Lan, J.Q., *et al.*, 2004. Migration through resolution cell compensation in ISAR imaging. *IEEE Geosci. Remote Sens. Lett.*, **1**(2):141-144. https://doi.org/10.1109/LGRS.2004.824766

Zhang, S.S., Xiao, B., Zong, Z.L., 2014. Improved compressed sensing for high-resolution ISAR image reconstruction. *Chin. Sci. Bull.*, **59**(23):2918-2926. https://doi.org/10.1007/s11434-014-0470-8